

CS observations of the hotspot at the S 155/Cepheus B interface

L. Olmi¹ and M. Felli²

¹ LMT Project and FCRAO, University of Massachusetts, 630 L.G.R.C., Amherst, MA 01003, USA (olmi@fcrao1.phast.umass.edu)

² Osservatorio Astrofisico di Arcetri, Largo E. Fermi 5, I-50125 Firenze, Italy (felli@arcetri.astro.it)

Received 17 February 1998 / Accepted 10 August 1998

Abstract. We have used the IRAM 30-m telescope to map, in the $J=2-1$, $J=3-2$ and $J=5-4$ rotational transitions of CS, the molecular *hotspot* located south-east of the Cepheus OB3 association, at the interface that divides the S 155 diffuse HII region from the Cepheus B molecular cloud. We have also used the FCRAO 13.7-m telescope to map the larger scale CS(2–1) emission. The $\simeq 1' \times 1'$ segment that has been mapped at higher spatial resolution with the 30-m telescope covers four radio continuum sources, one of which (source A) is a blister-type HII region. By using the CS molecule we analyse: *i*) the molecular density at the interface region and *ii*) the kinematics of the molecular gas at the front. The observations confirm that the blister has created a cavity at the edge of the molecular *hotspot* and is bounded on its sharp side by a dense molecular front in pressure equilibrium with the ionized gas. The near-IR star at the centre of the blister (A-NIR) is responsible for its ionization and for the heating of the *hotspot*.

Key words: HII regions – ISM: molecules – stars: formation – radio lines: ISM

1. Introduction

The Cepheus molecular cloud, at a distance of 725 pc, is a well known star forming region (Hartigan et al. 1986, Sargent 1977, 1979). The O and B stars of the Cepheus OB3 association are responsible for ionizing a large diffuse HII region (S 155), which lies at the interface between the large scale molecular cloud and the OB association (Sargent 1979).

The relationship between the Cep B molecular cloud and S 155 has been studied using radio continuum (Felli et al. 1978, and Testi et al. 1995, hereafter TOHTFG), recombination lines (Panagia & Thum 1981), combined far-infrared (FIR) and CO (Minchin et al. 1992, hereafter MWW), and optical and near-infrared (NIR) observations (Moreno-Corral et al. 1993, and TOHTFG). A summary of all these observations can be found in TOHTFG.

Here, we want to concentrate on a small region ($\sim 100''$) in S 155 close to Cep B, which is the hottest ^{12}CO component and is located to the NW edge of the molecular complex. MWW found

that the spatial distribution of the ^{12}CO emission in Cep B has an elephant trunk appearance with a peak brightness temperature of 48 K. The *hotspot* is close to a small bright HII region, which is believed to be ionized by an internal B1–B0.5 star rather than from the stars of the OB association (Felli et al. 1978, MWW). MWW proposed that the *hotspot* and the bright HII region are the product of sequential star formation due to shock compression of the molecular cloud induced by the radiation from HD217086, the brightest star of the Ceph OB3 association.

More recently, TOHTFG using NIR and high-resolution radio continuum observations were able to resolve this bright HII region into four distinct components (see Fig. 1): source A, which contains most of the radio flux and has a blister-type morphology, an extended ionization front (called the RIDGE), and two unresolved sources (B and C). NIR observations revealed a miniature stellar cluster, with three bright objects near the positions of the radio sources A, B and C. Source B is non-thermal (with $S_\nu \sim \nu^{-1.3}$) and its connection with the star forming complex is unclear. All available indications suggest a rather evolved nature of the blister HII region: no H_2O maser or molecular outflow are present and the near IR source located at its centre (called A-NIR) does not show any IR excess.

In this paper we focus on the *hotspot* (see Fig. 1) with slightly higher resolution molecular observations using a molecular species, CS, which allows to better define the morphology, physical parameters and kinematics of the high density molecular gas in a region of strong interaction between ionized and molecular gas.

The outline of the paper is the following: in Sect. 2 we give a brief description of the observations, and in Sect. 3 we describe the results. Finally, in Sect. 4, we draw our conclusions.

2. Observations

The multi-transition C^{32}S observations of the *hotspot* were carried out using the IRAM 30-m telescope on Pico Veleta in October 1996. We observed the CS $J = 2 - 1$, $3 - 2$ and $5 - 4$, with rest frequencies of 97.981, 146.969 and 244.936 GHz, respectively. The corresponding half power beam widths (HPBW) of the 30-m at those frequencies are $26''$, $18''$, and $12''$, respectively.

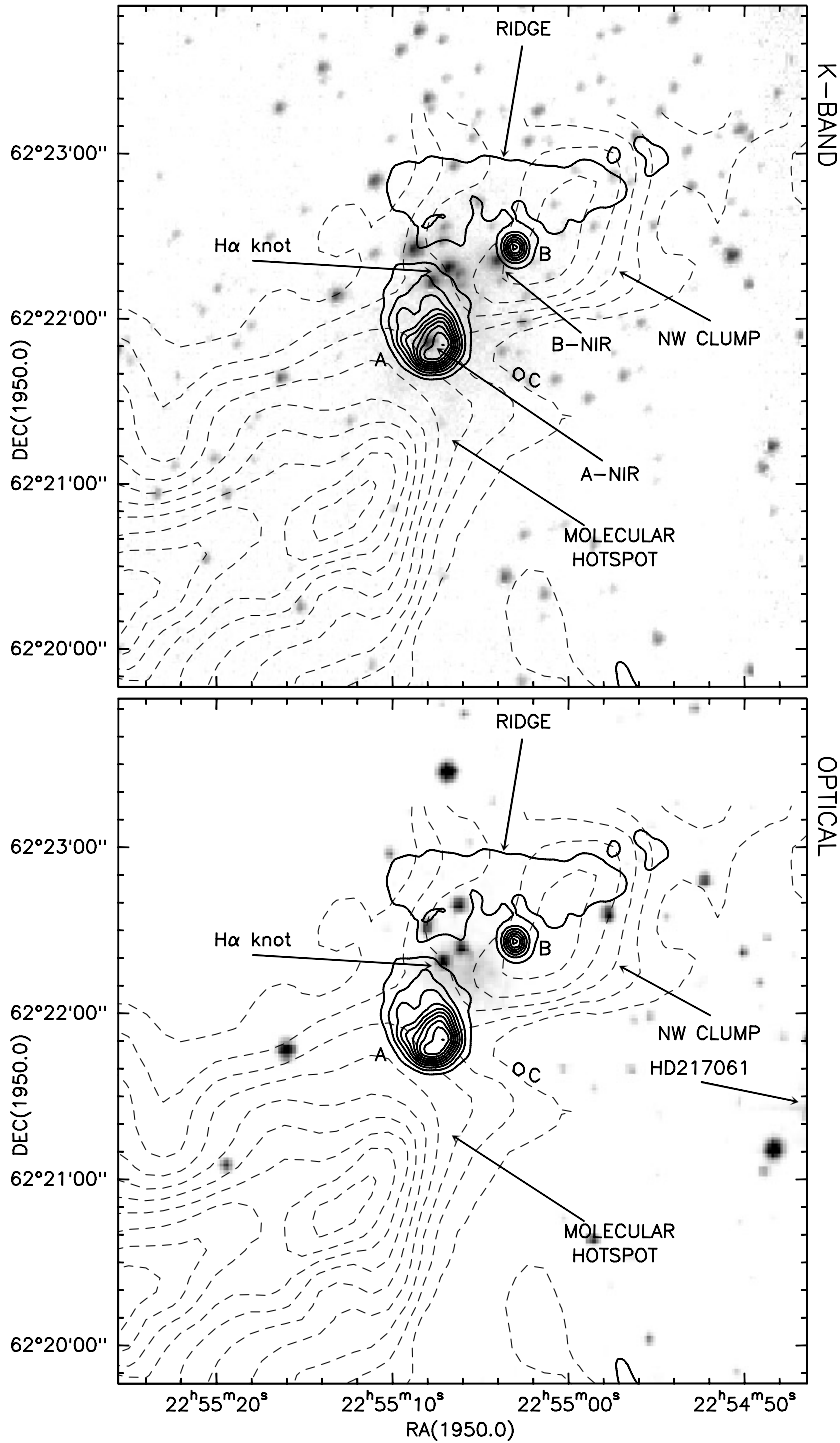


Fig. 1. K-band (*top panel*) and optical (*bottom panel*) images (grey scale, logarithmic in both images) overlaid with the FCRAO map (resolution $44''$) of the CS(2–1) integrated intensity (dashed contours), in the range -15 to -11 km s^{-1} , and with the VLA-D map (resolution $4''$) from TOHTFG (solid contours). The CS(2–1) levels vary from 0.2 to 2.2 by 0.2 K km s^{-1} , and the continuum emission is in the range from 0.3 mJy/beam to 7.5 mJy/beam. One of the brightest stars of the OB3 association, HD217061, is barely visible at the W edge of the map. The other bright member, HD217086, far more north, is not visible in this map.

The front-end receivers employed SIS mixers with system temperatures in the ranges $230 - 350$ K at 3 mm, $250 - 800$ K at 2 mm (in a few spectra $T_{\text{sys}} \sim 1700$ K), and about $650 - 3000$ K at 1.3 mm, after correction for atmosphere and telescope efficiency. Our spectrometers were two filter-banks with 1 MHz resolution (one of which was split into two parts to cover both the (2–1) and (3–2) lines) and two autocorrelators. The bandwidths used in the observations are listed in Table 1, together with the corresponding central frequencies and spectral resolutions.

The integration time used for the single-scan varied from 2 to 4 minutes in total power mode, and beam chopping was carried out by using the wobbler (i.e. a nutating secondary). The intensity scale in our spectra is given in main beam brightness temperature, T_{mb} . The achieved sensitivities in this scale for integration times varying from 12 min to 44 min were 0.03 K to 0.066 K. The flux density to main beam brightness temperature ratio for a point source, S_{ν}/T_{mb} , was 4.7 Jy/K (wavelength

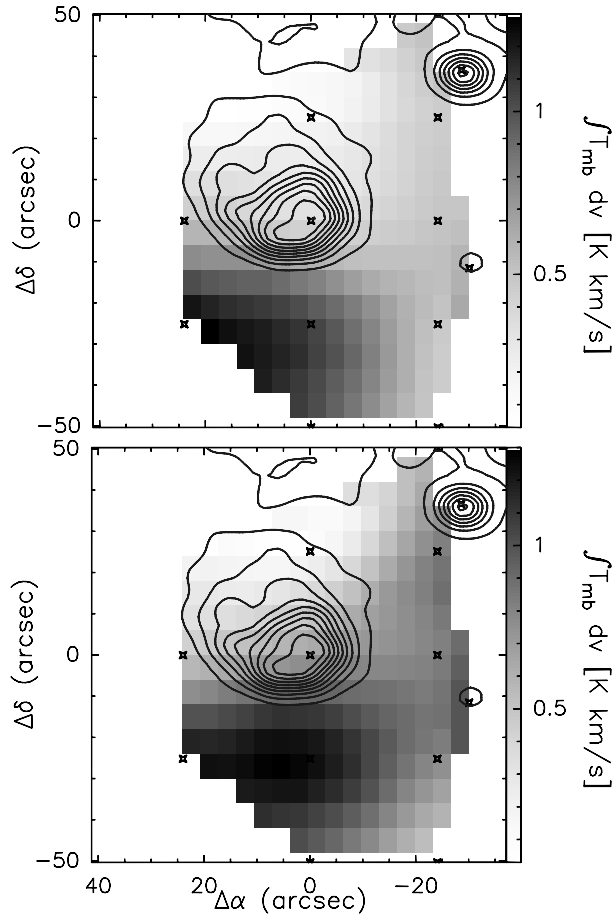


Fig. 2. IRAM 30-m maps of the CS integrated intensity (in the range -15 to -11 km s^{-1}) in K km s^{-1} , toward VLA source A of Cep B. The pointlike source B is visible in the NW corner of the map, whereas source C can be seen at position $(-30'', -10'')$. The grey scale corresponds to the CS(2–1) (*top panel*, $26''$ beam) and CS(3–2) emission (*bottom panel*, $18''$ beam). The small crosses represent the observed positions. The contour levels refer to the VLA-D continuum emission at 8.4 GHz, from TOHTFG, and their range is the same as in Fig. 1. Offsets are given with respect to the position of source A listed in Table 2

independent). The positions of source A and B (from TOHTFG) are listed in Table 2.

We obtained further data on the CS(2–1) transition in January 1998 with the 13.7-m telescope of the Five College Radio Astronomy Observatory¹ (FCRAO) in New Salem (U.S.A.), using the new SEQUOIA 32 element focal plane array, although for the present observations only 12 elements were actually used.

The integration time used for the single-scan was about 23 minutes in frequency switching mode, using a frequency throw of 4 MHz. The HPBW at the frequency of the CS(2–1) line of the FCRAO telescope is about $44''$, and the map was carried out using Nyquist sampling. The main beam efficiency used to

¹ The Five College Radio Astronomy Observatory is operated with support from the National Science Foundation and with permission of the Metropolitan District Commission

Table 1. Frequency setups used for the transitions observed: the first number is the frequency at which the spectrum was centred, the second indicates the bandwidth, and the third is the spectral resolution. All values are in MHz

Telescope	$J=2-1$	$J=3-2$	$J=5-4$
IRAM	97981; 256; 1	146969; 256; 1	244936; 512; 1
IRAM	97981; 70; 0.04	–	244936; 25; 0.1
IRAM	97981; 70; 0.08	146969; 70; 0.08	–
FCRAO	97981; 20; 0.02	–	–

Table 2. Coordinates of radio continuum sources A and B

Source	$\alpha(1950)$	$\delta(1950)$
A	22 55 07.201	62 21 50.0
B	22 55 03.103	62 22 25.0

convert the antenna temperature, T_A^* , to main beam brightness temperature is $\eta_{\text{mb}} = 0.45$.

3. Results

3.1. Morphology

3.1.1. FCRAO observations

The spatial distribution of the CS(2–1) emission shown in Fig. 1 resembles very closely the CO(3–2) map of MWW around the position of the *hotspot*. Our overlay clearly shows that source A has formed between the edge of the elephant trunk and another minor clump located NW of the HII region, and coincident with the RIDGE and source B. One can also note that the peak of the integrated intensity is not at the interface with the ionization front, but is located more SE and actually the elephant trunk has two distinct peaks.

As in the CO(3–2) map of MWW, the figure clearly shows the steep drop-off in emission at the molecular cloud edge. The bulk of the CS(2–1) emission is at velocities of -11.5 to -14.5 km s^{-1} , slightly blue-shifted relative to the CO(1–0) emission (Sargent 1977), and over a smaller velocity range than that observed by MWW in CO(3–2), who detected emission from -10 to -16 km s^{-1} . An interesting feature is that most of the emission from the NW clump is concentrated at velocities -13 to -14.5 km s^{-1} . The less clearly defined edge of the clump at these velocities may also be a further indication of disruption of the cloud edge, as suggested by MWW.

3.1.2. IRAM 30-m observations

Because of the weakness of the lines, CS was mapped by sampling at HPBW intervals (at 3 mm), for a total of 12 points in a map $\simeq 50'' \times 80''$, barely covering the region occupied by the sources A, B and C. In Fig. 2, the CS(2–1) and CS(3–2) integrated intensity maps are given, overlaid on the radio

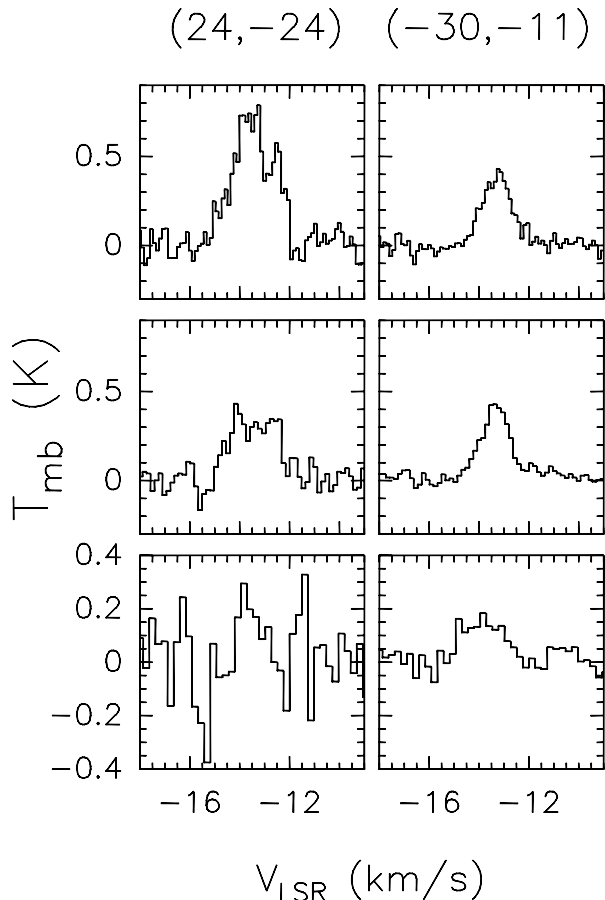


Fig. 3. IRAM 30-m spectra of CS towards two positions around source A: position (24, -24) (*left column*), and (-30, -11) (*right column*). The intensity scale is in main-beam brightness temperature. We show in the top row CS(2-1), in the middle CS(3-2), and in the bottom CS(5-4). The CS(5-4) spectra have been smoothed to a 0.24 km s^{-1} velocity resolution.

continuum map of TOHTFG. The signal-to-noise ratio in the CS(5-4) line was generally very low, so we shall not show a map of this line.

Fig. 2 clearly shows a noticeable anticorrelation between the ionized gas of the blister and the molecular gas in the *hotspot*. There is a sharp increase in integrated intensity (and, as we shall see, also in column density) to the south of the sharpest side of source A, proving that the blister HII region has cleared of molecular gas the ionized region and that the sharp side of the blister faces a dense wall of molecular material in the *hotspot*, just at the edge of the elephant trunk.

Both CS(2-1) and CS(3-2) channel maps show that the strongest emission comes from the S-SE region, where the sharp edge of the molecular cloud is very clearly defined. The sharpness of the emission is particularly evident for blue-shifted velocities ($V_{\text{lsr}} < -14 \text{ km s}^{-1}$), whereas at more red-shifted velocities the emission is smoothly distributed and it also begins to appear along a NW-SE direction, including the centre of source A.

The spectra of the CS(2-1), (3-2) and (5-4) lines towards two different positions are presented in Fig. 3 to show the relative

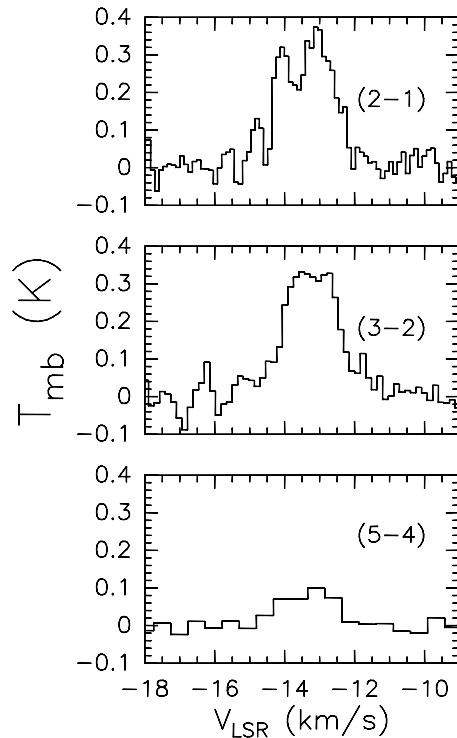


Fig. 4. IRAM 30-m spectra of CS towards VLA source B: position (-28.5, 35). We show in the top panel CS(2-1), in the middle CS(3-2), and in the bottom CS(5-4). The CS(5-4) spectrum has been smoothed to a 0.49 km s^{-1} velocity resolution.

strength of the emission. The spectra on the left side were taken at position (24, -24) (hereafter offsets in arcseconds with respect to the position of source A will be given) where both CS(2-1) and (3-2) reach their maximum integrated intensity, whereas the spectra on the right side of Fig. 3 were taken at position (-30, -11), where the maximum of CS(5-4) integrated intensity has been observed. The results of Gaussian line fits (V_{LSR} , FWHM, T_{mb}) and the line integrated intensity, $\int T_{\text{mb}} dV$, of the spectra taken at position (-30, -11) and at the nominal position of source B (-28.5, 35) are given in Table 3.

In Fig. 4 we also present spectra of the CS lines observed towards VLA source B. The most interesting feature is the dip in the CS(2-1) line, at a velocity of -13.6 km s^{-1} , which could be the result of some moderate self-absorption. A spectrum taken at position (-24, +48), i.e. only about 13 arcsec away from the peak of source B, also shows a dip at the *same* velocity. These two spectra averaged together give a stronger evidence for the presence of self-absorption. Although more sensitive observations are needed to confirm it, we can exclude that source B is the cause of absorption. In fact, the brightness temperature at 3 mm, extrapolated from the observed flux at 3.6 cm, would only be 0.17 K even under the assumption of free-free emission, or much lower with the observed non-thermal spectral index, thus too small compared to the excitation temperature of CS. Most probably the absorption comes from cooler foreground gas at a slightly blue-shifted velocity with respect to the systemic velocity.

Table 3. Observed (IRAM 30-m) line parameters toward source A ($-30, -11$), corresponding to the peak CS(5–4) integrated intensity, and source B, ($-28.5, 35$). The integrated intensity has been estimated in the range -15 to -11 km s $^{-1}$, and the errors are formal 1σ values and do not take into account the calibration uncertainty.

Line	A				B			
	V_{LSR} (km s $^{-1}$)	FWHM (km s $^{-1}$)	T_{mb} (K)	$\int T_{\text{mb}} dV$ (K km s $^{-1}$)	V_{LSR} (km s $^{-1}$)	FWHM (km s $^{-1}$)	T_{mb} (K)	$\int T_{\text{mb}} dV$ (K km s $^{-1}$)
CS(2–1)	-13.27 ± 0.03	1.42 ± 0.08	0.39 ± 0.02	0.59 ± 0.02	-13.36 ± 0.04	1.89 ± 0.09	0.33 ± 0.06	0.64 ± 0.03
CS(3–2)	-13.33 ± 0.02	1.40 ± 0.06	0.41 ± 0.03	0.65 ± 0.03	-13.23 ± 0.04	1.80 ± 0.09	0.35 ± 0.03	0.67 ± 0.03
CS(5–4)	-13.9 ± 0.1	1.90 ± 0.20	0.17 ± 0.03	0.23 ± 0.03	-13.3 ± 0.2	1.70 ± 0.40	0.10 ± 0.03	0.17 ± 0.04

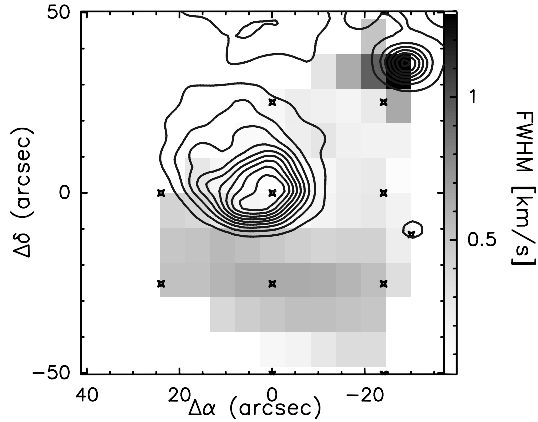


Fig. 5. Map of the velocity width, in km s $^{-1}$, of CS(2–1) (IRAM 30-m data). The contour levels of the VLA map are the same as in Fig. 1.

3.2. Kinematics

The FWHM of all CS lines varies in the range $\sim 1 - 2$ km s $^{-1}$, which means that at the gas kinetic temperature of ~ 60 K believed to be representative of the *hotspot* (MWW), the CS lines are dominated by turbulent or large scale motions.

It is of interest to consider the kinematic relation between the ionization front of source A and the molecular cloud. This can be done by overlaying a map of the CS line-width with one of the continuum emission, as in Fig. 5. The FWHM of CS(2–1) has a minimum at the centre position and increases S and SE of the HII region. At positions (24, -24) and (0, -24), i.e. at the direct interface between the molecular cloud and the sharp side of the blister, the CS(2–1) and (3–2) spectra seem to have 2 components (separated by $\simeq 1.1$ km s $^{-1}$, see Fig. 3), with the strongest component being the blue-shifted one. It thus looks as if the line FWHM is higher along the molecular cloud sharp edge.

The line-width also reaches a high value ($\Delta V = 1.9 \pm 0.1$ km s $^{-1}$) at the position of source B. At this position CS(2–1) and (3–2) have essentially the same kinematic parameters, while CS(5–4) shows some deviations: it has a wider FWHM and it is also slightly blue-shifted with respect to the lower excitation lines. The amount of the shift is 0.57 km s $^{-1}$, i.e. more than two resolution channels in the CS(5–4) smoothed spectrum, and is even more pronounced in two other CS(5–4) spectra.

This result would seem to suggest that the (5–4) transition is tracing a different volume of gas at this location.

There are variations in the spatial distribution of the line V_{lsr} 's. The most red-shifted CS(2–1) line was observed towards the centre of source A, with $V_{\text{lsr}} = -12.96 \pm 0.05$ km s $^{-1}$ (i.e., very close to the systemic V_{lsr} of Cep B). Other positions with lines having red-shifted central velocities are found in the NW–W region, whereas in the S–SE region spectra are more intense at blue-shifted velocities, with $V_{\text{lsr}} = -13.85 \pm 0.05$ km s $^{-1}$ at position (24, 0).

We also note that CS(2–1) at (0, 0) has a slightly non-Gaussian profile, with peak at $V_{\text{lsr}} = -12.6$ km s $^{-1}$. A *two*-line Gaussian fit with a fixed line-width of 1.1 km s $^{-1}$ leads to a blue-shifted component at $V_{\text{lsr}} = -13.75$ km s $^{-1}$, almost coincident with the velocity of the single line at position (24, 0), and a red-shifted component at $V_{\text{lsr}} = -12.82$ km s $^{-1}$, almost coincident with the velocity of the red-shifted component observed in the spectra at positions (24, -24) and (0, -24), as shown in Fig. 6.

We therefore suggest that the expansion of the HII region and its associated shocks have accelerated the molecular gas along the line of sight both toward and away from us by as much as ± 0.5 km s $^{-1}$. The emission in the NW–W region probably comes from gas which is not directly at the blister skin, and whose velocity is $\simeq -13$ km s $^{-1}$, close to the systemic velocity. The gas observed towards the centre of source A has the most red-shifted velocity and an asymmetric profile suggesting that we are looking at emission which is partly produced at the molecular cloud interface with the blister, on the side *receding* from us, in agreement with the bright H α appearance of this region. More southward, the line of sight intercepts the very interface between the ambient gas and the expanding I-front, causing the gas to be accelerated both towards and away from us and giving rise to the observed sharp edge in the blue-shifted emission and to the largest value of the FWHM.

3.3. LVG model

Information on local density is provided by the relative intensity of the three CS rotational transitions. From the observed line temperatures we can derive average densities along the line of sight using a “Large Velocity Gradient” (or LVG) model, assuming uniform density and temperature.

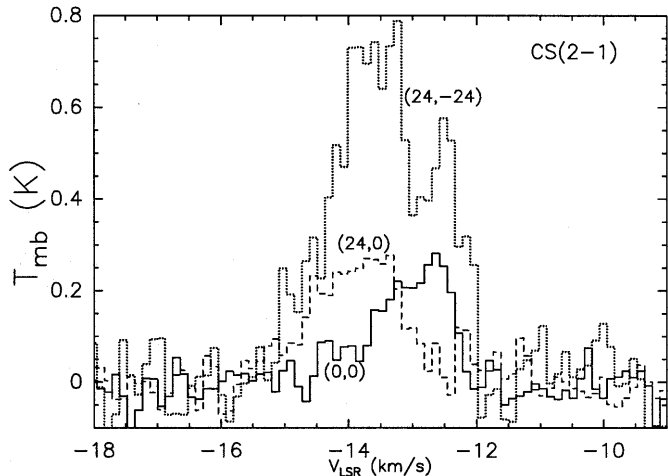


Fig. 6. IRAM 30-m spectra of CS(2–1) towards positions (0, 0) (solid line), (24, 0) (dashed line), (24, –24) (dotted line).

It is important to note that because of the limited number of observed points in the CS maps obtained at the 30 m telescope, and also because of the fact that the CS(5–4) transition is both undersampled and very weak, we considered inappropriate to attempt any spatial resampling of the CS(5–4) (and also 3–2) map to the same angular resolution as in the (2–1) map. On the other hand, we did not have an *a priori* model of the source. All things considered, we then decided to proceed in the following way: we selected spectra in the SE and NW regions, and made a Gaussian fit to their *average* to compare the resulting peak line temperature with the output of the LVG models. We also selected those positions throughout the *whole* CS(5–4) map with the best RMS noise, and averaged all CS transitions at these same positions.

In the LVG models we assumed a temperature of 60 K, a unity filling factor for the position-averaged spectra, and adopted the CS-H₂ collision rates of Green & Chapman 1978 (M. Walmsley, private communication). In this way we avoid the introduction of any arbitrary hypothesis on the source structure, as it would be implied by adjusting the filling factor. The results for the averaged spectra are shown in Fig. 7, and are summarized in Table 4. The excitation temperature, T_{ex} , is about 6–7 K in the SE region but it increases up to 17 K for the CS(2–1) transition in the NW region. The CS optical depth is always $\ll 1$.

The LVG results seem to suggest the presence of a density gradient between the SE and NW regions of the 30 m maps, although we caution the reader about possible residual beam-coupling effects in the three wavelength bands observed. These effects should be less important when the *average* characteristics of the interface region are considered, as in the case of Fig. 7, at the bottom.

The CS abundance to velocity gradient ratio of 2.5×10^{-12} km s⁻¹ pc⁻¹ derived from the LVG model is somewhat lower than that usually found in a variety of molecular clouds (see e.g. Linke & Goldsmith 1980) and would require a low CS abundance

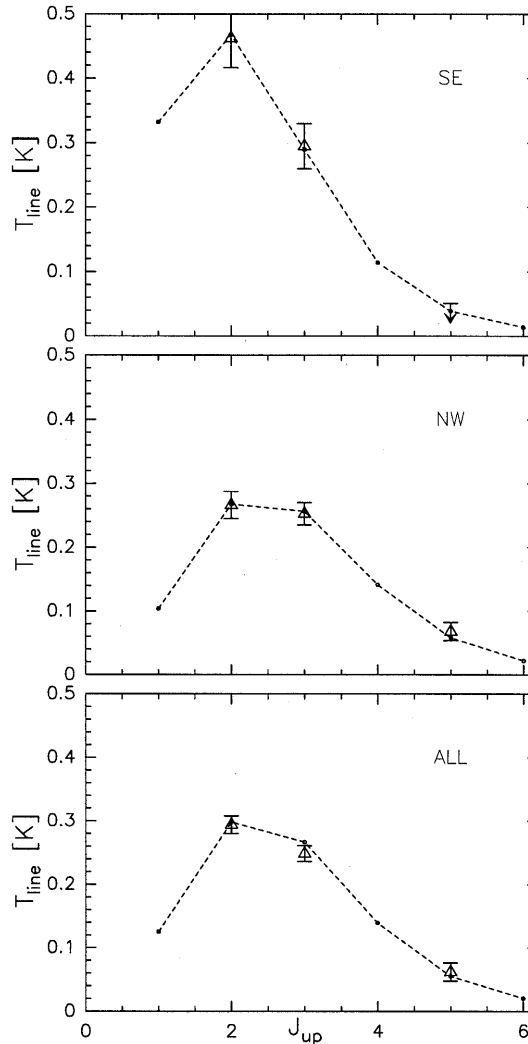


Fig. 7. The LVG model results (small circles and dashed line), after a Gaussian fit to the position-averaged line profiles (triangles), in the SE (top panel), NW (middle panel), and throughout the whole (bottom panel) interface regions. T_{k} was fixed at 60 K and the hydrogen density and CS abundance to velocity gradient ratio are listed in Table 4

Table 4. Results of an LVG model applied to the position-averaged spectra of CS, for $T_{\text{k}} = 60$ K.

Region	n $\times 10^5$ (cm ⁻³)	$X(\text{CS})/(dv/dr)$ $\times 10^{-12}$ (km s ⁻¹ pc ⁻¹) ⁻¹	χ^2
SE	0.6	12	0.25
NW	1.7	1.9	0.53
ALL	1.4	2.5	2.4

and/or a high velocity gradient. It can be a further indication that CS is depleted in the region close to the ionization front.

Assuming uniform excitation conditions across the line profile, and uniform hydrogen density in the region of emission, then the CS column densities can be written as:

$$N(\text{CS}) = 3.3 \times 10^{18} \left[\frac{X(\text{CS})}{dv/dr} \right]_{\text{peak}} n_{\text{H}_2} \Delta V_{\text{FWHM}} \quad (1)$$

where a Gaussian line profile has been taken (Linke & Goldsmith 1980). The column density is in units of cm^{-2} , the fractional abundance per unit velocity gradient is in units of $(\text{km s}^{-1} \text{pc}^{-1})^{-1}$, the molecular hydrogen density is in cm^{-3} , and the line width in km s^{-1} . Using the values of Table 4 we derive CS column densities of a few times 10^{12}cm^{-2} .

These results are in good agreement with the approximated estimates that can be obtained assuming that the optical depth of the CS transitions is only moderately thick and that the beam filling factor is unity, and then using the following formula:

$$N_{\text{tot}} = 7.54 \cdot 10^{11} \frac{T_{\text{ex}} [\text{K}]}{J^2} \exp \left\{ \frac{B [\text{K}] J(J-1)}{T_{\text{ex}}} \right\} \int T_{\text{mb}} dV [\text{K km s}^{-1}] \quad [\text{cm}^{-2}] \quad (2)$$

where B [K] is the CS rotational constant, measured in degrees K, and J is the quantum number of the upper level.

Fig. 2 shows that much less molecular gas is present along the line of sight, when we scan the region progressively from the SE to the NW, with a strong anticorrelation between radio continuum/optical emission and molecular emission. If, for the sake of simplicity, we also assume that the excitation temperature of the gas is uniform throughout the observed region, then we see that Fig. 2 is also a representation of the spatial distribution of column density.

In the framework of the LVG approximation each velocity within the line profile can be interpreted as a physically independent region of the cloud. Then, variation of density along the line of sight can show up as variations in the intensity ratio of two lines. The CS(3–2) to CS(2–1) intensity ratio monotonically decreases from $\gtrsim 1$ at blue-shifted velocities, to less than 1 at more red-shifted velocities in the S–SW region, suggesting density variations along the line of sight in this direction, while it is constant in other parts.

The constancy of the CS line intensity ratio towards the centre and in the NW–W region, together with low optical depths, would require that these CS emitting regions have nearly uniform density along the line of sight. Furthermore, if the optical depths are less than one (e.g., with a CS abundance to velocity gradient ratio $X(\text{CS})/(dv/dr) \lesssim 5 \times 10^{-10} (\text{km s}^{-1} \text{pc}^{-1})^{-1}$ at $T_k > 40$ K), then the line ratio is independent of $X(\text{CS})$ and is basically an indicator of molecular hydrogen density, with a value > 1 suggesting densities $\gtrsim 2 \times 10^5 \text{cm}^{-3}$.

The fact that CS(5–4) is observed at least towards some positions, and has an appreciable fraction ($\simeq 14 - 27$ %) of the intensity of the (2–1) line, is a further indication of the presence of high density gas.

4. Discussion and conclusions

The CS(2–1) and CS(3–2) peak line temperatures (~ 0.5 K) observed in the *hotspot* are much lower than those found with similar observations in a sample of dense molecular clumps where massive stars are just being formed, in which values as high as 10 – 12 K have been observed (Cesaroni et al., in preparation). Considering that these lines require densities $\gtrsim 10^6 \text{cm}^{-3}$ to

be thermalized, this suggests that in later evolutionary stages, as seems to be the case for the *hotspot*, the molecular densities are lower. This confirms that the high brightness temperature observed in ^{12}CO by MWW (48 K) is due to high temperature (~ 60 K), lower density molecular gas located close to a heating source.

The ratio of CS(3–2) to ^{13}CO antenna temperature (using the ^{13}CO value of MWW) is 0.08, about a factor 5 lower than the mean value found in the Cesaroni et al. sample. This may suggest that CS is depleted close to the ionization front, as also suggested by the LVG model.

Our higher resolution observations of the CS(2–1), (3–2) and (5–4) rotational transitions of the *hotspot* have confirmed that the blister-type HII region has evacuated a cavity and formed a sharp dense front at the edge of an extended molecular cloud, particularly intense in the S–SW part. The morphology confirms that A-NIR is the stellar source responsible for the heating source of the dust emitting in the far IR and, in turn, of the *hotspot*, as discussed by MWW. To estimate hydrogen densities we position-averaged the spectra in different regions, to mitigate the effects of undersampling at the higher frequency CS transitions, and compared the resulting spectra with a set of LVG models at fixed temperature. We thus found densities of order of $1 - 3 \times 10^5 \text{cm}^{-3}$, and total CS column density $\sim 10^{12} \text{cm}^{-2}$.

The mean electron density in source A is $3.7 \times 10^2 \text{cm}^{-3}$ (TOHTFG). Assuming the standard temperature in an HII region of 10^4 K and using the molecular gas temperature of 60 K, the pressure equilibrium density in the molecular front is $6 \times 10^4 \text{cm}^{-3}$. The molecular density in the larger scale molecular cloud are much smaller, of order of 10^3cm^{-3} (MWW). The higher value at the front is close to the values derived from the LVG analysis. The density increase must be produced by shock compression ahead of the ionization front.

At the southern edge of source A, both the integrated line intensity (i.e., column density) and the line-width of CS(2–1) and (3–2) are enhanced. This effect is more pronounced at blue-shifted velocities, where the integrated intensity shows a sharp edge, almost bordering source A. Line profiles show some degree of asymmetry, consistent in some cases with a two-components Gaussian fit. We interpret these effects as an indication of shocked molecular gas in a shell around the blister being accelerated away and towards us.

The line profiles associated with the NW part of our maps are consistent with a single component, and emission is observed at less blueshifted velocities. This molecular gas is thus likely to be associated with the remnant of the dense clump from which A-NIR originally formed. The coincidence of the NW clump with source B still leaves open the query if this non-thermal source is associated with it or not.

Acknowledgements. We are grateful to A. Sievers and A. Greve for carrying out the IRAM-30m observations. We are also grateful to R.L. Snell for helpful advices, to R. Cesaroni for critically reading the manuscript, and to an anonymous referee for useful comments.

References

- Felli M., Tofani G., Harten R.H., Panagia N., 1978, A&A 69, 199
Green S., Chapman S., 1978, ApJS 37, 169
Hartigan P., Lada C.J., Stocke J., Tapia S., 1986, AJ 92, 1155
Linke R.A., Goldsmith P.F., 1980, ApJ 235, 437
Minchin N.R., Ward-Thompson D., White G.J., 1992, A&A 265, 733,
(MWW)
Moreno-Corral M.A., Chavarria-K. C., de Lara E., Wagner S., 1993,
A&A 273, 619
Panagia N., Thum C., 1981, A&A 98, 295
Sargent A.I., 1977, ApJ 218, 736
Sargent A.I., 1979, ApJ 233, 163
Testi L., Olmi L., Hunt L. et al., 1995, A&A 303, 881, (TOHTFG)